# Multidimensional Perovskites for High Detectivity Photodiodes

Document Version:
Publisher's PDF, also known as Version of Record (includes final page, issue and volume numbers)

Please check the document version of this publication:

• A submitted manuscript is the version of the article upon submission and before peer-review. There can be important differences between the submitted version and the official published version of record. People interested in the research are advised to contact the author for the final version of the publication, or visit the DOI to the publisher's website.
• The final author version and the galley proof are versions of the publication after peer review.
• The final published version features the final layout of the paper including the volume, issue and page numbers.

[Link to publication](#)

# Multidimensional Perovskites for High Detectivity Photodiodes

*Riccardo Ollearo, Alessandro Caiazzo, Junyu Li, Marco Fattori, Albert J. J. M. van Breemen, Martijn M. Wienk, Gerwin H. Gelinck, and René A. J. Janssen\**

Low-dimensional perovskites attract increasing interest due to tunable optoelectronic properties and high stability. Here, it is shown that perovskite thin films with a vertical gradient in dimensionality result in graded electronic bandgap structures that are ideal for photodiode applications. Positioning low-dimensional, vertically-oriented perovskite phases at the interface with the electron blocking layer increases the activation energy for thermal charge generation and thereby effectively lowers the dark current density to a record-low value of $5 \times 10^{-9}$ mA cm$^{-2}$ without compromising responsivity, resulting in a noise-current-based specific detectivity exceeding $7 \times 10^{12}$ Jones at 600 nm. These multidimensional perovskite photodiodes show promising air stability and a dynamic range over ten orders of magnitude, and thus represent a new generation of high-performance low-cost photodiodes.

## 1. Introduction

Hybrid perovskites have been extensively investigated in opto-electronic devices, such as solar cells, light-emitting diodes (LEDs), and photodiodes. Among them, low-dimensional perovskites have emerged as attractive materials because of their structural diversity and higher stability compared to

R. Ollearo, A. Caiazzo, J. Li, M. M. Wienk, G. H. Gelinck, R. A. J. Janssen
Molecular Materials and Nanosystems and Institute of Complex Molecular Systems
Eindhoven University of Technology
P.O. Box 513, Eindhoven 5600 MB, The Netherlands
E-mail: r.a.j.janssen@tue.nl
M. Fattori
Integrated Circuits
Department of Electrical Engineering
Eindhoven University of Technology
P.O. Box 513, Eindhoven 5600 MB, The Netherlands
A. J. J. M. Breemen, G. H. Gelinck
TNO at Holst Centre
High Tech Campus 31
Eindhoven 5656 AE, The Netherlands
R. A. J. Janssen
Dutch Institute for Fundamental Energy Research
De Zaale 20, Eindhoven 5612 AJ, The Netherlands

their 3D counterpart.[1–3] While 3D hybrid perovskites adopt a cubic structure consisting of $[BX_6]^{4-}$ corner-sharing octahedra, with the organic cation fitting in the voids between the inorganic units, 2D or quasi-2D perovskites consist of a number ($n$) of inorganic sheets sandwiched between organic spacers, such as butylammonium (BA) or phenethylammonium (PEA). Such cations are too bulky to fit in the octahedral voids, so they effectively slice the perovskite framework and form quantum-well structures with a bandgap and exciton binding energy that depends on the value of $n$.[4] Small $n$-values correspond to 2D ($n = 1$) or quasi-2D ($n \leq 5$) perovskites with a bandgap energy inversely proportional to $n$, while large $n$-values approaching infinity describe a quasi-3D or 3D perovskite with the conventional optoelectronic properties widely described in the literature.[5] When solution-processing quasi-2D perovskites, typically a range of structural phases with different $n$-values are formed in the films while drying. As a consequence, these films often display a 2D–3D gradient, with 2D or quasi-2D phases located at the bottom and 3D phases at the top air interface,[6,7] resulting in a complex, multidimensional material. As $n$ is coupled with the energy bandgap, a 2D–3D gradient results in a bandgap gradient that can be used beneficially to increase the detectivity of perovskite photodiodes (PPDs), as we will show below.

To develop PPDs with high specific detectivity ($D^*$), low noise current ($i_n$) should be combined with high photosensitivity.[8] In previous work, we have shown that high-detectivity photodiodes can be achieved by minimizing the dark current density ($J_D$), and thus $i_n$, of 3D PPDs by using appropriate blocking layers.[9] When charge injection is suppressed, $J_D$ and $i_n$ are determined by thermal charge generation at the interface between the electron-blocking layer (EBL) and the perovskite layer, and exponentially depend on the energy offset between the highest occupied molecular orbital (HOMO) of the EBL ($E_{HOMO, EBL}$) and the conduction band minimum (CBM) of perovskite ($E_{C, PVK}$), that is, $\Phi = E_{C, PVK} - E_{HOMO, EBL}$. Increasing $\Phi$ reduces $J_D$ and $i_n$, and thus improves $D^*$. 3D perovskites, however, offer limited solutions in controlling energy levels to maximize $\Phi$. A wide-bandgap perovskite could potentially increase $\Phi$, but at the cost of a narrower spectral response window and higher instability under illumination.[10] On the contrary, multidimensional perovskites are a versatile candidate material that allows tuning of energy

**ADVANCED
SCIENCE NEWS**

www.advancedsciencenews.com

**ADVANCED
MATERIALS**

www.advmat.de

levels at the interface with the transport layers by optimizing their 2D–3D gradient composition. Their bandgap gradient along the thickness of such films enables an upshift of the CBM at the interface with the EBL, yielding to an increased energy offset between the HOMO of the EBL and the conduction band of the perovskite, de facto increasing $\Phi$. As a result, such perovskites could be exploited to achieve higher $D^*$ compared to 3D perovskite devices. The absorption profile and thus spectral response would remain relatively unaltered, with only a slight blueshift.

Although quasi-2D perovskites have been broadly employed in solar cells and light-emitting diodes,[11–15] their use for photodiode applications has been seldom investigated.[16–20] Moreover, a comprehensive study correlating the design of low-dimensional phases with the device characteristics both in dark and light is lacking.

In this work, we investigated several quasi-2D perovskite compositions in PPDs. We outline the key conditions to maximize the photodiode performance. By means of composition and spacer engineering, we control the 2D–3D gradient and demonstrate that multidimensional perovskite films can effectively reduce $J_D$. By analyzing the temperature-dependence of $J_D$, we confirmed that $J_D$ is the result of thermal charge generation process at the EBL interface with a high-bandgap 2D or quasi-2D phase. We found that vertical-oriented perovskites are necessary to obtain an external quantum efficiency (EQE) > 80% and fast response times. Employing the quasi-2D perovskites with proper gradient direction and crystal orientation in combination with deep-HOMO EBL, we fabricated PPDs with record-low $J_D$ of $5 \times 10^{-9}$ mA cm$^{-2}$, noise-current based specific detectivity exceeding $7 \times 10^{12}$ Jones, fast microsecond response times, and a linear photo-response over more than 8 orders of magnitude of light intensity. Hence, interface engineering with low-dimensional perovskites leads to photodiodes with performance that is on par with traditional inorganic semiconductors.

## 2. Results and Discussion

We recently demonstrated that in 3D PPDs the interface with the EBL is very critical.[9] $J_D$ decreases exponentially with $\Phi$, which is the energy offset between 3D perovskite CBM and HOMO of the EBL. With the aim to increase $\Phi$ even further, we here investigate 2D–3D graded perovskites as active layers in PPDs. This is illustrated in **Figure 1**. In Figure 1a, a multi-dimensional perovskite is shown, consisting prevalently of 2D ($n = 1$) or quasi-2D phases ($n \leq 5$) at the bottom of the film, and 3D phases ($n \approx \infty$) at the top. This material possesses a bandgap ($E_g$) gradient along the thickness of the film, with higher $E_g$ and CBM at the bottom.[21] The introduction of 2D phases at the EBL interface thus results in a potential increase of $\Phi$ (Figure 1b).

The formation of a 2D–3D gradient is controlled by the perovskite fabrication method. We have recently shown how solvent-precursors interactions are crucial in determining the phase distribution of a quasi-2D perovskite film.[22] By following a similar solvent engineering approach, we fabricated 2D–3D graded perovskite films in which we deliberately controlled the distribution of structural phases and their crystal orientation, to obtain $n$-values ranging from 1 to 5 and either parallel or perpendicular crystals. In particular, we used two largely studied organic spacers, that is, butylammonium (BA) and phenethylammonium (PEA). The stoichiometry of the precursor solutions was set to form $BA_2MA_3Pb_4I_{13}$ (⟨$n$⟩ = 4) and $BA_2MA_4Pb_5I_{16}$ (⟨$n$⟩ = 5), in the case of BA, and $PEA_2MA_3Pb_4I_{13}$ (⟨$n$⟩ = 4) for PEA. The choice of such a value of $n$, and not for example smaller $n$-values that could further increase $\Phi$, was dictated by considerations about the narrowing of spectral response for the wider optical bandgap associated with the smaller $n$ and about crystal orientation, as will be discussed below. In addition, two 3D perovskites with comparable bandgap, that is, $FA_{0.66}MA_{0.34}PbI_3$ (FAMA) and $Cs_{0.05}(FA_{0.83}MA_{0.17})_{0.95}Pb(I_{0.83}Br_{0.17})_3$ (CsFAMA), were also investigated. The fabrication details are described in the Experimental Section. All perovskite films were spin coated on an indium tin oxide (ITO) patterned glass substrate covered with an edge cover layer (SiN) and poly[bis(4-phenyl)(2,4,6-trimethylphenyl)amine] (PTAA) as EBL. On top of the perovskite layer, a bilayer of thermally-evaporated $C_{60}$ and bathocuproine (BCP) acts as HBL, while Ag is the back electrode (Figure 1a).

The composition and phase distribution of the perovskite films was characterized using photoluminescence (PL)



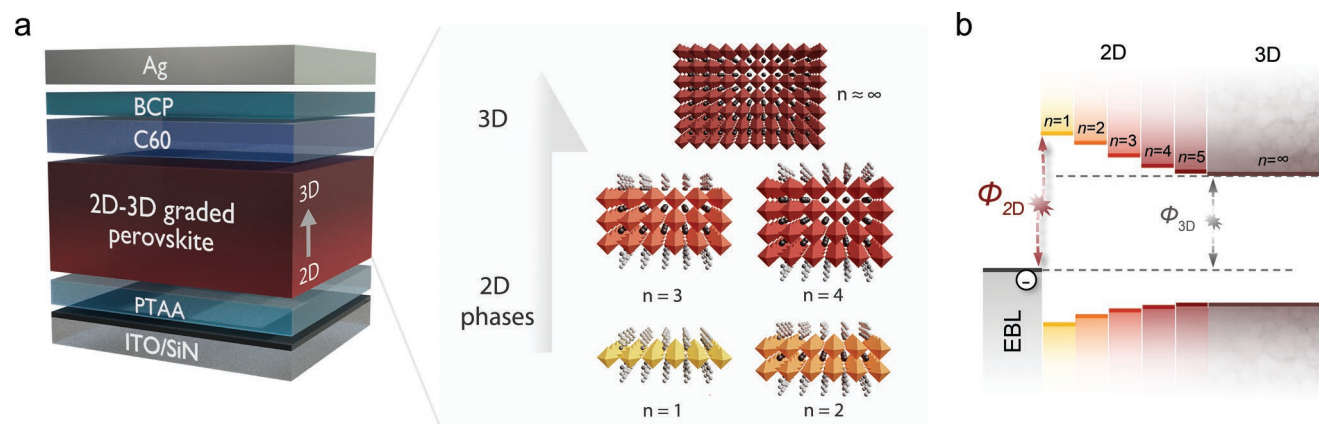**Figure 1.** a) Layer stack of the perovskite photodiode architecture with focus on the 2D–3D gradient, where low-dimensional and 3D perovskite phases are illustrated. b) Schematic energy band diagram for a 2D–3D graded perovskite layer considering a Type I alignment between low-dimensional phases. The difference between conduction band and HOMO level of EBL corresponds to the energy barrier $\Phi$ for thermal charge generation.

**ADVANCED**
**SCIENCE NEWS**
www.advancedsciencenews.com
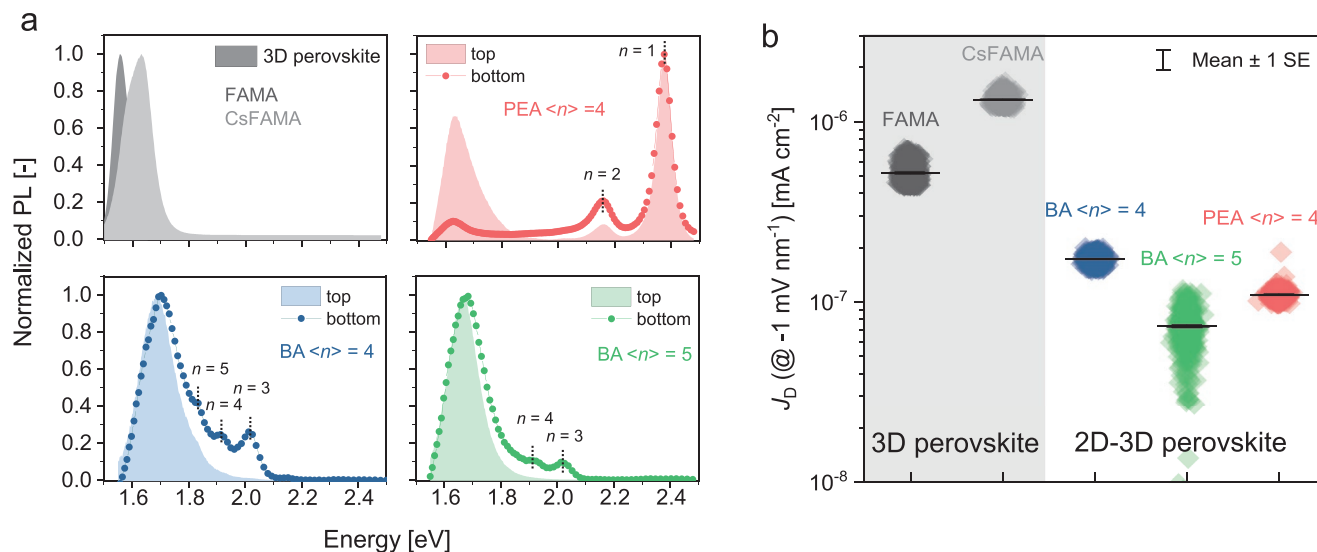
**ADVANCED**
**MATERIALS**
www.advmat.de

**Figure 2.** a) Normalized steady-state PL spectra of the 3D and quasi-2D perovskite films recorded with excitation (405 nm) and detection at the top (air/perovskite) and bottom (substrate/perovskite) sides. b) Variation of the dark current density during 300 s, measured under a constant electric field of $-1$ mV nm$^{-1}$ for the different perovskite photodiodes.

measurements (**Figure 2**a). The 3D perovskites have similar PL spectra with an emission peak at 1.55 and 1.63 eV for FAMA and CsFAMA, respectively. All quasi-2D perovskite films display a dimensionality gradient. When exciting the film with light of 405 nm (penetrating only the first ≈40 nm out of ≈200 nm layer thickness) and detecting PL from the top side, the films emit at ≈1.7 eV, indicating the presence of a 3D perovskite. Upon exciting and detecting at the bottom side, additional emission peaks, indicative of structural phases with different $n$-values and of the presence of a 2D–3D gradient, are observed. It is worth mentioning, however, that the 3D emission peak at 1.7 eV that dominates the spectrum even when exciting at the bottom side, is due to ultrafast carrier migration from quasi-2D to 3D phase, as commonly reported in the literature.[23] In the case of BA, we observe the formation of structural phases with $n$ between 3 and 5 (for BA $<n> = 4$) and between 3 and 4 (for BA $<n> = 5$) at the bottom of the film. The emission peaks of these quasi-2D phases are found at 2.02, 1.91, and 1.82 eV for $n = 3$, 4, and 5, respectively. The different BAI:MAI:PbI$_2$ precursor ratios between $<n> = 4$ and $<n> = 5$ cause a change in crystallization kinetics and are likely behind these differences in phase distribution. On the contrary, PEA-based perovskite films possess a large amount of $n = 1$ (2.37 eV) and 2 (2.16 eV) at the bottom, and a 3D perovskite mixed with the same low-dimensional phases at the top. Although PL spectroscopy is not a quantitative technique, we emphasize that the absence (or minor presence) of a 3D emission peak in the bottom-excitation PL spectrum of PEA $<n> = 4$, indicates a drastic majority of small-$n$ phases, which are unable to transfer to 3D phases. We further analyzed the morphology of quasi-2D perovskite films via scanning-electron microscopy (SEM) and confirmed that all films are closed and without pinholes (Figure S1, Supporting Information).

We next measured the reverse dark current of the quasi-2D PPDs and compared it with that of 3D PPDs (Figure 2b). The $J_D$ was measured over time (300 s) by applying a constant electric

field of $-1$ mV nm$^{-1}$. In the case of BA $<n> = 4$, $<n> = 5$ and PEA $<n> = 4$, the time-averaged mean $J_D$ is $2 \times 10^{-7}$, $6 \times 10^{-8}$, and $1 \times 10^{-7}$ mA cm$^{-2}$, respectively. Notably, BA and PEA $<n> = 4$ display a negligible spread of current densities with time, whereas it is larger for BA $<n> = 5$ for reasons that we have yet to identify. The mean $J_D$ values are reproduced over several devices (Figure S2, Supporting Information). These values are almost one order of magnitude lower than the ones measured for 3D perovskites CsFAMA and FAMA ($1 \times 10^{-6}$ and $6 \times 10^{-7}$ mA cm$^{-2}$, respectively) and are ranked among the lowest reported in the literature for quasi-2D and 3D PPDs.[8,9,16,17,24]

Furthermore, we investigated the energetic correlation of quasi-2D phases with $\Phi$ by analyzing the thermal activation energy ($E_a$) of $J_D$ for three PPDs (FAMA, BA $<n> = 4$ and PEA $<n> = 4$). $E_a$ was determined by using temperature-dependent $J_D$ measurements. For all devices, $J_D$ shows an Arrhenius-type behavior, with $E_a$ increasing from 0.87 eV (3D FAMA) to 1.16 eV (BA $<n> = 4$, with $n = 3$, 4, 5) and 1.29 eV (PEA $<n> = 4$, with $n = 1$, 2) (Figure S3, Supporting Information). The highest temperature activation is thus observed in the PPD with the lowest dark current. Quasi-2D perovskites exhibit a significantly higher $E_a$, by 0.3–0.4 eV, compared to that of the 3D perovskite, which is consistent with an increase of $\Phi$ caused by the high-bandgap low-dimensional phases at the EBL interface, in line with Figure 1b. Determining $E_a$ for BA $<n> = 5$ turned out to be difficult due to the low current level ($J_D < 10^{-7}$ mA cm$^{-2}$).

To further investigate the influence of low-dimensional phases at the EBL interface on $\Phi$, we fabricated a multidimensional PPD with reverse 3D–2D graded perovskite ($<n> = 4$). Here, by using cyclohexylmethylammonium (CMA) as organic spacer,[25] we promote the formation of 2D phases on the top of the film, and 3D ones at the bottom (**Figure 3**a). X-ray diffraction (XRD) displays a peak at 3.87° corresponding to the (020) plane of $n = 2$ (Figure 3b).[26] PL emission spectra confirm the reversed dimensionality gradient, showing a 3D emission peak at 1.62 eV with excitation from the bottom side,
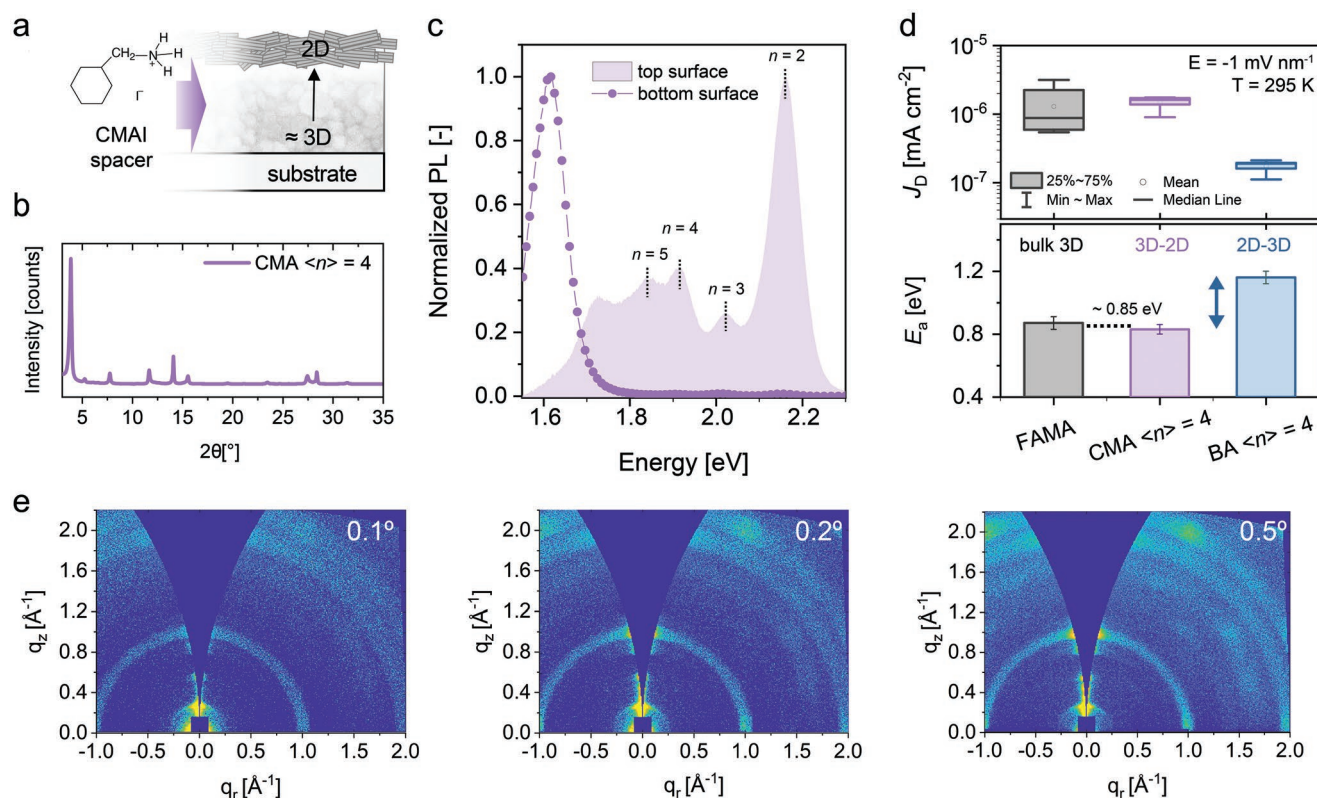
**Figure 3.** a) Schematic illustration of the 3D–2D gradient obtained by using cyclohexylmethylammonium iodide as organic spacer. b) XRD pattern for $(CMA)_2MA_3Pb_4I_{13}$ ($<n>$ = 4). c) Normalized steady-state PL spectra of the same film as in (b) measured with excitation (405 nm) and detection at the top (air/perovskite) and bottom (substrate/perovskite) sides. d) Statistical distribution of $J_D$ (top) and measured activation energy $E_a$ (bottom, whiskers are standard error) for bulk 3D, 3D–2D graded and 2D–3D graded perovskite photodiodes. In the boxplots (top), statistical information is provided in the legend. e) Angle-dependent GIWAXS patterns for $(CMA)_2MA_3Pb_4I_{13}$ ($<n>$ = 4) recorded with incidence angles of 0.1°, 0.2°, and 0.5°.

whereas multiple emission peaks related to quasi-2D phases are observed with excitation from the top side (Figure 3c). The main emission peak from the top side is found at 2.1 eV, suggesting the dominant presence of an $n$ = 2 phase in agreement with XRD. Additionally, we employed angle-dependent grazing-incidence wide-angle X-ray scattering (GIWAXS) to gain depth-sensitive information on the 3D-2D graded perovskite crystalline structure. When using a 0.1° or 0.2° incident angle, the X-rays penetrate only the top surface of the film, whereas at larger angles (0.5°) the whole film thickness is probed. The top surface (measured with 0.1° incidence angle) of the perovskite film exhibits an intense Bragg spot at $q_z$ = 0.29 Å$^{-1}$ and a weak scattered ring at 1 Å$^{-1}$. The peak at 0.29 Å$^{-1}$ corresponds to the abovementioned (020) plane of an $n$ = 2 phase oriented parallel to the substrate. The weak ring at 1 Å$^{-1}$ results from the (111) plane of a Ruddlesden–Popper phase. At higher incidence angles (0.2° and 0.5°), the ring becomes more intense, because of the contribution of the (100) plane of the 3D phases, and a Bragg spot in the out-of-plane direction appears, indicating preferential crystal orientation. Moreover, the out-of-plane cuts display peaks at $q_z$ = 0.23 and 0.18 Å$^{-1}$, corresponding to an interplane spacing of 27 and 36 Å, consistent with $n$ = 3 and 4 phases, respectively (Figure S4, Supporting Information),[27] which become more intense with increasing incident angle, indicating the appearance of larger-$n$ phases moving towards the bottom of the film.

By integrating the CMA $<n>$ = 4 reverse graded perovskite as active layer in a photodiode with the same p-i-n device stack as before, we found $J_D$ to be $2 \times 10^{-6}$ mA cm$^{-2}$ (Figure 3d) at room-temperature, with an $E_a$ of 0.87 eV. These numbers are close to the values of $J_D$ of $6 \times 10^{-7}$ mA cm$^{-2}$ and $E_a$ of 0.83 eV of 3D FAMA and differ significantly from those of 2D–3D bottom-side graded perovskites, that is, 1.16 and 1.29 eV. These results suggest that the EBL-perovskite interface in a 3D–2D top-side graded perovskite is by all means similar to 3D FAMA and CsFAMA. Low-dimensional phases are thus less effective in decreasing $J_D$ when located at the HBL interface.

In multidimensional perovskites, the response of the material to light is strongly affected by the crystal orientation of the films.[12] Previous studies have reported that small-$n$ phases such as $n$ = 1 or 2 preferentially orient horizontally, that is, parallel to the substrate. Larger-$n$ phases ($n$ = 3–5) tend to orient vertically, that is, perpendicular to the substrate.[28] Through GIWAXS measurements, we determined the crystal orientation of the 2D–3D graded perovskites and we compared them to 3D FAMA, which only exhibits a scattered ring at 1 Å$^{-1}$, consistent with a randomly oriented crystalline structure (**Figure** 4a). BA-templated perovskites with $<n>$ = 4 or 5 display vertical orientation of the crystals (Figure 4b and Figure S5, Supporting Information), as confirmed by the intense Bragg spot at 1 Å$^{-1}$ that corresponds to the (111) plane of Ruddlesden–Popper or (110) of 3D perovskites. This is in line with the PL
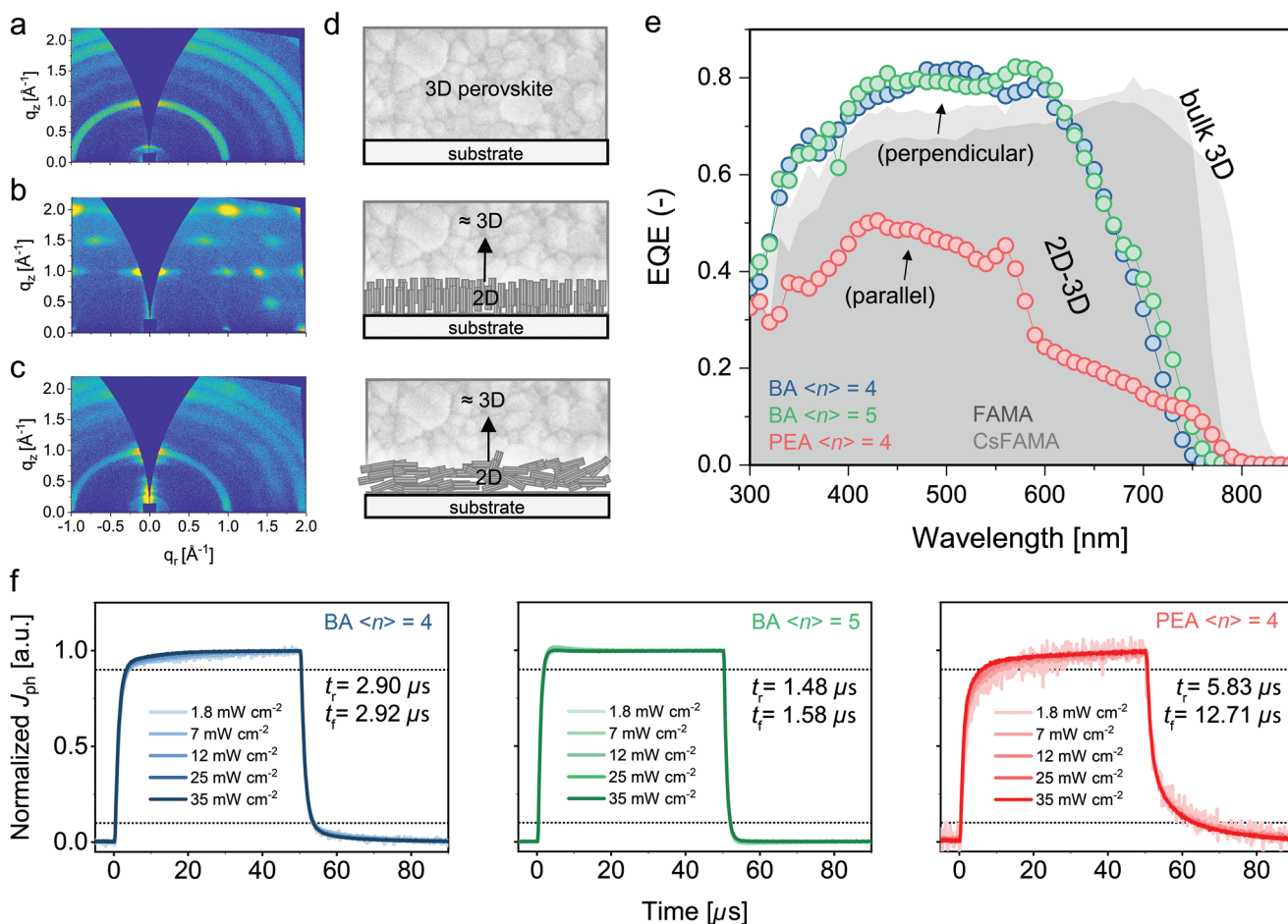
**Figure 4.** a) GIWAXS pattern for FAMA, b) GIWAXS pattern for BA $<n>$ = 4, c) GIWAXS pattern for PEA $<n>$ = 4. d) Schematic illustration of random oriented 3D (top) and perpendicular- (middle) or parallel- (bottom) oriented 2D–3D graded perovskite films. e) EQE spectra for 3D, perpendicular-, and parallel- oriented 2D–3D graded PPDs. f) Normalized transient photocurrent response upon light pulses (50 μs duration, 540 nm) with different light intensities for BA $<n>$ = 4, BA $<n>$ = 5, and PEA $<n>$ = 4. Rise (and fall) time, that is, time for response vary from 10% (90%) to 90% (10%), are also reported.

characterization results described above, where only phases with $n$ = 3, 4, and 5 appeared together with a bulk 3D perovskite, and with XRD patterns, which show diffraction peaks only for the abovementioned planes (Figure S4, Supporting Information). In the GIWAXS pattern of PEA $<n>$ = 4, we observe Bragg spots at 0.28 and 0.38 Å$^{-1}$ along the $q_z$ direction, which are assigned to $n$ = 1 and 2 phases parallel-oriented to substrate, and overall a lower degree of vertical orientation (Figure 4c). XRD patterns also confirm the presence of such phases with peaks at 5.4° and 3.9°, corresponding to the (002) planes of $n$ = 1 and (020) planes of $n$ = 2, respectively (Figure S6, Supporting Information). Using GIWAXS, we can therefore distinguish between perpendicular-oriented and parallel-oriented films that are schematically illustrated in Figure 4d. BA-based perovskites with $<n>$ = 4 and 5 are perpendicular-oriented, while PEA $<n>$ = 4 is parallel oriented.

We measured both EQE (Figure 4e) and response speed (Figure 4f) of the photodiodes described above. Light is incident from the bottom side. The randomly oriented bulk 3D shows a sharp onset at the bandgap above 800 nm, and a maximum EQE approaching 80%. The perpendicular-oriented 2D–3D

graded perovskites possess a favorable crystal orientation for charge transport, and this is reflected in the EQE > 80% in the visible region of the EQE spectrum. The onset, however, is shallower as a result of low volumetric amounts of pure 3D perovskite phases, in agreement with UV-vis-NIR spectra (Figure S7, Supporting Information).[22] The parallel-oriented perovskite displays a sharper 3D onset because of higher amounts of 3D perovskites.[22] The values of EQE, nonetheless, are halved to 40% (with few peaks at 50%), due to unfavorable crystal orientation for charge transport and possibly poor film morphology. This also reflects in the spectral responsivity of the PPD, which consistently drops from 0.4 A W$^{-1}$ for the perpendicular-oriented BA-templated perovskites to 0.2 A W$^{-1}$ for the parallel-oriented PEA-based quasi-2D perovskite (Figure S8, Supporting Information).

The PPD response times, measured using 50 μs wide light pulses at 540 nm wavelength for various intensities, are shown in Figure 4f. The response speed was found to be independent of light intensity in the perpendicular-oriented perovskites, with microsecond rise and decay times (i.e., 2.9 and 1.5 μs for BA $<n>$ = 4 and 5, respectively). A longer decay time (≈12 μs) is

**ADVANCED**
**SCIENCE NEWS**

www.advancedsciencenews.com

**ADVANCED**
**MATERIALS**

www.advmat.de

observed instead for parallel-oriented PEA $<n>$ = 4, together with a light intensity dependent rise time that varies between ≈6 and 10 µs, as an indication of sub-optimal charge transport. Together with changes in EQE, these findings outline the importance of crystal orientation in 2D–3D graded perovskites for fast and efficient collection of photogenerated charges, while having negligible impact on $J_D$ (Figure 2b). Perovskite films with vertical-oriented crystals and, more importantly,

without parallel-oriented small-$n$ phases are therefore preferred as they suppress $J_D$ while retaining high and fast responsivity.

To improve PPD performance, we combined the multidimensional 2D–3D graded perovskites with vertical-oriented crystals, that is, BA $<n>$ = 4 and 5, with a deep HOMO EBL, that is, a mixed PTAA:poly(4-butyl-$N,N$-diphenylaniline) (poly-TPD) layer (**Figure 5**). This approach enables EQEs ≈80% and spectral responsivity (SR) ≈0.4 A W$^{-1}$ (Figure S9, Supporting
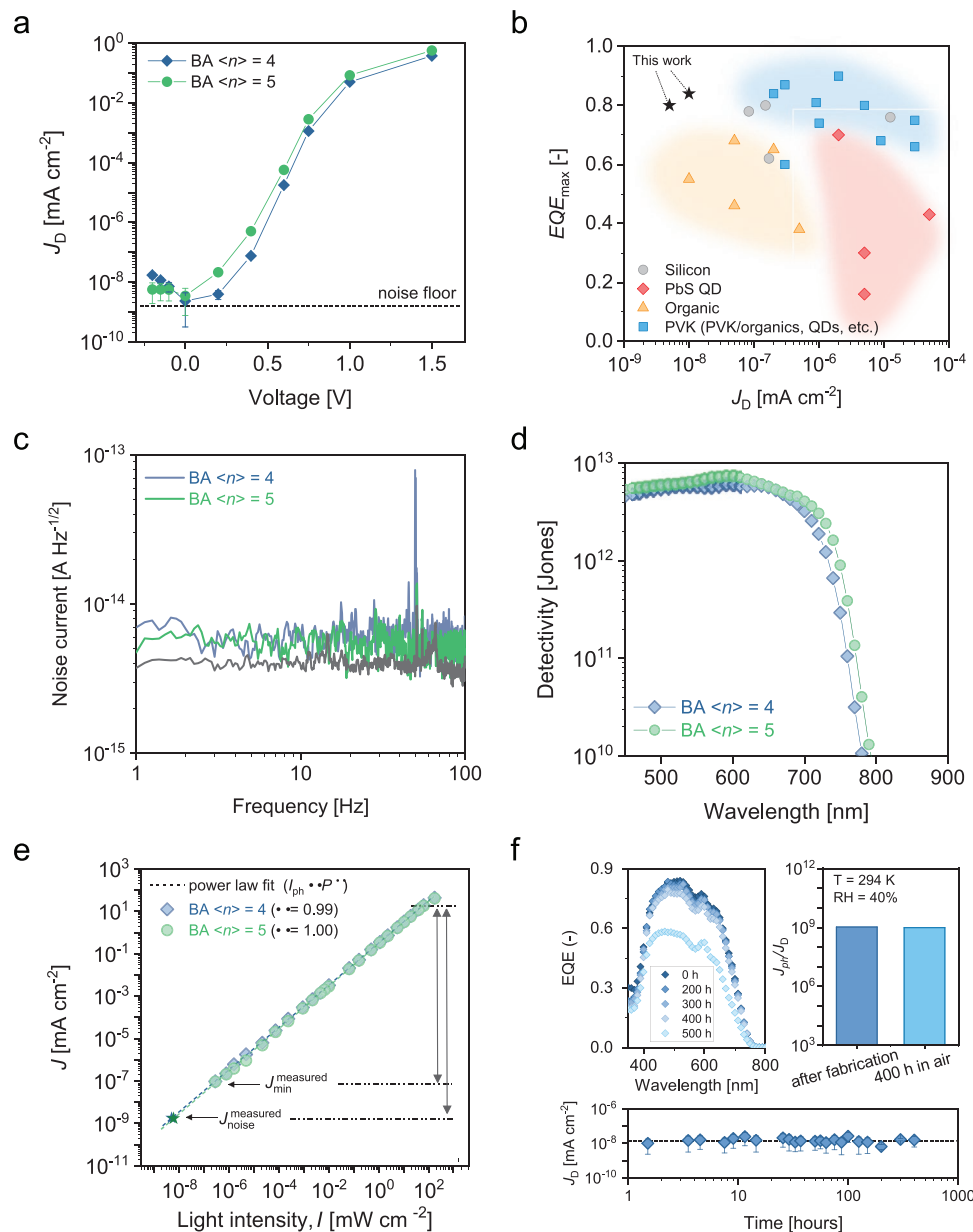


**Figure 5.** a) $J$–$V$ characteristics in dark; from −0.2 to +0.6 V, $J$–$V$ have been reconstructed from constant voltage measurements over time at discrete biases. Whiskers represent standard deviation. b) Plot of maximum EQE versus minimum $J_D$ comparing our PPDs with state-of-art solution-processed photodiodes and commercial silicon. For each device, $J_D$ at $V$ = −0.2 V is reported Further details are in the Supporting Information. c) Noise current spectral density as a function of frequency measured at −0.2 V for the best devices. Each spectrum is obtained with an average of 15 measurements. Harmonics with large amplitude in the spectrum are due to powerline interference. Black line represents the noise floor of the setup (≈4 × 10$^{-15}$ A Hz$^{-1/2}$). d) Specific detectivity of the photodiodes versus wavelength under reverse bias (−0.2 V). e) Photocurrent, $J_{ph}$, measured at −0.2 V for a broad range of light intensities (540 nm). Lines denote a linear fit, with $\alpha$ the power law exponent equal to unity. f) Stability in air (RH 40%) of BA $<n>$ = 4 PPD after >400 h, expressed in terms of EQE (top left), $J_{ph}/J_D$ ratio (top right), and $J_D$ over time (bottom). $J_{ph}$ is integrated from the EQE spectrum at $V$ = 0 V, $J_D$ is measured at constant voltage measurements over time at discrete biases (symbols and whiskers represent mean values and standard deviation).

**ADVANCED
SCIENCE NEWS**

www.advancedsciencenews.com

**ADVANCED
MATERIALS**

www.advmat.de

Information). The interfacial energy $\Phi$ of such combinations is in fact maximized beyond that of PPDs employing only 2D–3D perovskites due to deep EBL HOMO energy ($\approx$−5.45 eV for PTAA:poly-TPD compared to −5.2 eV for PTAA[9]) and the $J_D$ is suppressed to extremely low values. A reproducible and record-low $J_D$ of $1 \times 10^{-8}$ mA cm$^{-2}$ and $\approx 5 \times 10^{-9}$ mA cm$^{-2}$ at −0.2 V was measured for BA $\langle n \rangle$ = 4 and 5, respectively (Figure 5a; Figure S10, Supporting Information) based on constant voltage measurements over time at discrete biases (Figure S11, Supporting Information). Such $J_D$ values represent the lowest dark current density reported for a PPD (Figure 5b; Figure S12 and Table S1, Supporting Information). Compared to other photodiodes, $J_D$ is more than ten times lower than that of most commercial Si and at least more than five times lower than the best performing organic PDs.[29–32] The noise current $i_n$, measured at −0.2 V in the frequency interval $f$ = 1–100 Hz is shown in Figure 5c. We observe a frequency-independent $i_n$ behavior (with no evidence of $1/f$ dependence) with outstanding values of current noise spectral density of 5.5 and $6.5 \times 10^{-15}$ A Hz$^{-1/2}$ for BA $\langle n \rangle$ = 5 and 4, respectively. Combined with the high EQE at 600 nm, this results in a maximum noise-current based specific detectivity $D^*$ of the photodiodes, that is, derived using $D^* = $ SR $(AB)^{1/2}$ $i_n^{-1}$ with $A$ = 0.01 cm$^2$ and $B$ = 1 Hz, of $\approx 7.5 \times 10^{12}$ (BA $\langle n \rangle$ = 5) and $6 \times 10^{12}$ (BA $\langle n \rangle$ = 4) Jones (Figure 5d). The shot noise-limited specific detectivity ($D^*_{shot}$), that is, under the assumption of predominating and limiting shot noise, of these PPDs amounts to $\approx 2 \times 10^{14}$ Jones (Figure S13, Supporting Information). The photocurrent ($J_{ph}$) as function of light intensity ($I_{light}$) of both devices is shown in Figure 5e. $J_{ph}$ increases linearly over nine orders of light intensity, with a slope of $\alpha$ = 0.99 and 1.00 for BA $\langle n \rangle$ = 4 and $\langle n \rangle$ = 5, respectively. This corresponds to a linear dynamic range (LDR = 20 log $(J_{ph,upper}/J_{ph,lower})$) of the photodiodes, that is, the span of the light intensity range within which the device output is linear to the incident light intensity, of $\approx$169 dB. At a light intensity of 175 mW cm$^{-2}$, the photocurrent does not scale linearly with $I_{light}$ anymore, which is more visible when plotting $R = J_{ph}/I_{light}$ instead of $J_{ph}$ (Figure S14, Supporting Information). The value of $J_{ph}$ at $I_{light}$ = 175 mW cm$^{-2}$ is therefore taken as $J_{ph,upper}$. The lower limit of LDR is governed by the minimum light intensity that could be produced repeatedly and constantly by our equipment. When considering the measured $J_{noise}^{measured}$ resulting from $i_n$ as $J_{ph,lower}$[16,33,34] the linearity range extends to more than ten orders of magnitude, corresponding to LDR > 200 dB.

Finally, we performed preliminary stability tests by exposing the BA $\langle n \rangle$ = 4 PPD, to ambient air (with relative humidity (RH) = 40% and $T$ = 295 K). We tested therefore its environmental stability without intentional encapsulation or protection layers. As shown in Figure 5f the photodiode maintained its low $J_D$ value of $\approx 1 \times 10^{-8}$ mA cm$^{-2}$ and high EQE ($\approx$80%) for 400 h with no appreciable decay (<4% for EQE). The $J_{ph}/J_D$ ratio remained therefore high, $\approx 10^9$. Approaching 500 h, the EQE decreases to 60%, indicating device degradation. As only the device area covered with the electrode shows a change of color (turning yellow) in the film, whereas the perovskite layer remains brown in the uncovered areas, we believe that degradation is caused by interaction between the electrode material (Ag) and the perovskite layer. Proper encapsulation will likely lead to even longer device stability.

In summary, we outlined key requirements for the design and integration of multidimensional perovskites in photodiodes for record-low dark current density, broad sensitivity to light intensity, and high specific detectivity. Through the study of several quasi-2D perovskites, we demonstrated how the distribution of low-dimensional structural phases, gradient direction, and crystal orientation impact the main figures of merit of a photodiode. Overall, we found that while the formation of a 2D–3D gradient and its direction help to minimize dark current, vertical orientation of quasi-2D perovskite films is also crucial to achieve high performance PPDs. Our work provides a comprehensive study of low-dimensional perovskites in PPDs and shows that multidimensional structuring is an accessible route to fabricate high detectivity and stable photodiodes.

## 3. Experimental Section

*Materials*: All materials were purchased from commercial sources and used without further purification unless otherwise mentioned. PbI$_2$ (99.99%) was purchased from TCI Chemicals, all the organic salts for perovskites were purchased from GreatCell Solar, all the solvents were bought from Sigma Aldrich.

*Perovskite Deposition*: Solution preparation and device fabrication were performed in an N$_2$-filled glovebox. FA$_{0.66}$MA$_{0.34}$PbI$_3$ (FAMA) was prepared via two-step spin coating according to a previous publication from our group.[35] First, a 1.2 M PbI$_2$ solution was spin coated on the EBL at 3000 rpm for 30 s. Then, the organic solution made of 0.31 M FAI and 0.16 M MAI in isopropanol was spin coated at 3000 rpm for 60 s. The perovskite films were thermally annealed at 100 °C for 30 min.

Cs$_{0.05}$(FA$_{0.83}$MA$_{0.17}$)$_{0.95}$Pb(I$_{0.83}$Br$_{0.17}$)$_3$ (CsFAMA) was prepared via one-step spin coating according to previously published research.[36] First, PbI$_2$ and PbBr$_2$ were dissolved in separate vials in dimetylformamide/dimethyl sulfoxide (DMF/DMSO) 4:1 (concentration is 1.5 M). Then, solutions of FAPbI$_3$ and MAPbBr$_3$ were prepared by mixing the lead solutions described above with FAI and MABr in equimolar ratio. Finally, FAPbI$_3$ and MAPbBr$_3$ were mixed in the ratio 5:1, followed by addition of 5% (by volume) CsI (1.5 M in DMSO). The perovskite precursor was spin coated at 1000 rpm for 10 s, followed by 6000 rpm for 20 s; 200 µL of chlorobenzene were poured onto the spinning substrate 5 s before the end of the spin coating process. The perovskite films were annealed at 100 °C for 45 min.

Quasi-2D perovskites with nominal formula R$_2$MA$_{n-1}$Pb$_n$I$_{3n+1}$ were prepared by mixing the organic spacer (BAI or PEAI), MAI, and PbI$_2$ in the ratio 2 : $n$−1 : $n$ in DMF:DMSO mixtures, with the concentration of PbI$_2$ set at 1 M. BA- and CMA-based perovskites were processed from a DMF:DMSO 20:1 solvent mixture, whereas the PEA-based perovskite was processed from DMF:DMSO 4:1 The precursor solutions were spin coated at 5000 rpm for 45 s, followed by thermal annealing at 100 °C for 10 min.

*Device Fabrication*: Indium tin oxide (ITO) (135 nm) was sputtered on glass and structured to form a bottom electrode via photolithography. SiN (50 nm) was deposited and patterned via dry etch to cover the perimeter of the ITO electrodes to reduce undesirable leakage paths.[37] Prior to deposition of the EBLs, a 30 min UV-ozone treatment was performed on the substrates. PTAA (3 mg mL$^{-1}$ in toluene) was spin coated at 5700 rpm for 30 s, followed by thermal annealing at 100 °C for 10 min. PTAA:polyTPD (10 mg PTAA, 10 mg polyTPD in 1 mL *o*-dichlorobenzene) was spin coated at 2500 rpm for 40 s, followed by thermal annealing at 135 °C for 35 min. C$_{60}$ (20 nm, SES Research), BCP (8 nm, Lumtec), and the Ag top electrode (100 nm) were thermally evaporated under high vacuum ($\approx$10$^{-7}$ mbar).

*Material Characterization*: PL spectra were measured by using an Edinburgh Instruments FLSP920 double-monochromator luminescence

spectrophotometer. UV–vis–NIR spectra were measured by using a PerkinElmer Lambda 1050 UV–vis–NIR spectrophotometer. XRD patterns were measured by using a Bruker 2D phases (Cu Kα, $\lambda$ = 1.5406 Å) in the range 3–35° with a step size of 0.02° and collection time of 1 s. 2D GIWAXS measurements were performed with a Ganesha 300XL+ system from JJ X-Ray equipped with a Pilatus 300K detector (pixel side 172 μm × 172 μm). The X-ray source was a Genix 3D Microfocus sealed tube X-ray Cu-source with integrated monochromator. The wavelength used was 1.5408 Å, the sample-to-detector distance was set to 115.4 mm.

*Device Characterization*: Room temperature dark current density was measured in an $N_2$-filled glovebox through manual probes connected to an Agilent 4155C semiconductor parameter analyzer. For an accurate determination of $J_D$, a constant reverse voltage bias was applied over time to eliminate unwanted charging effects. For temperature dependent $J_D$ measurements, the device was placed under vacuum ($10^{-4}$ mbar) in a cryostat chamber and connected to a Keithley (2636A) source meter, while temperature was controlled using liquid nitrogen and a LakeShore 336 temperature controller. The transient photocurrent (TPC) was measured using a digital oscilloscope (Tektronix TDS5052B) and green light pulses (540 nm) generated by a LED driven by a wave-function generator (Agilent 33250A). Optical focal lens and a circular aperture (1 mm in diameter) by Thorlabs were used to guide the light signal. Within the same setup, the photocurrent response of the PPD was measured employing two different green LEDs to emit at high and low light intensity regions that were calibrated with a reference silicon photodiode (Thorlabs FDS100). The custom-made setup for EQE measurements consisted of a tungsten-halogen lamp, a monochromator (Oriel, Cornerstone 130), a chopper, a pre-amplifier (Stanford Research Systems SR570), and a lock-in amplifier (Stanford Research Systems SR830 DSP). The devices were transferred in the setup through a $N_2$-filled box equipped with a quartz window, on which a circular aperture (1 mm diameter) was applied. EQE signal was calibrated with a reference silicon solar cell. The standard deviation of this setup is <0.005 electron/photon (in the range 350–1050 nm of wavelengths). Noise measurements were performed in a battery-powered current to voltage conversion readout circuit developed with off-the-shelf components. The setup is arranged in a metal enclosure to shield the device from electromagnetic interference and keep it in dark conditions. The photodiode (active area of 1 $mm^2$) was connected by means of two probes and triaxial cables to a trans-impedance amplifier (TIA) implemented with the operation amplifier analog devices (ADA4530). The device was biased by applying an adjustable DC voltage source to the non-inverting terminal of the TIA. The output of the TIA was fed to an active bandpass amplifier (building using Analog Devices AD8065 operational amplifier) and finally read out by a dynamic signal analyzer (HP35670A).

*Statistical Analysis*: The $J_D$'s shown in Figure 2b were time-averaged over 300 s. Mean values and standard error (SE) are shown with horizontal bars. A boxplot for $J_D$ of different devices is shown in Figure S2, Supporting Information. The boxplot in Figure 3d shows the statistical distribution of $J_D$ for bulk 3D, 3D–2D graded, and 2D–3D graded perovskite photodiodes. The whiskers in Figure 5a,f represent the standard deviation.

## Supporting Information

Supporting Information is available from the Wiley Online Library or from the author.

## Acknowledgements

## Conflict of Interest

The authors declare no conflict of interest.

## Author Contributions

R.O. and A.C. contributed equally to this work. R.O., A.C. fabricated the devices, A.C. designed and characterized the perovskite material, and R.O. performed analysis of the photodiodes. J.L. performed GIWAXS measurements. M.F. developed the noise setup. A.J.J.M.B. optimized the processes of PPD substrates. R.O., A.C., R.A.J.J., and G.H.G. planned the research and interpreted the data. A.C., R.O. wrote the manuscript with help of R.A.J.J. and G.H.G. All authors commented on it.

## Data Availability Statement

The data that support the findings of this study are available from the corresponding author upon reasonable request.

## Keywords

[1] X. Li, J. M. Hoffman, M. G. Kanatzidis, *Chem. Rev.* **2021**, *121*, 2230.

[2] F. Zhang, H. Lu, J. Tong, J. J. Berry, M. C. Beard, K. Zhu, *Energy Environ. Sci.* **2020**, *13*, 1154.

[3] G. Grancini, M. K. Nazeeruddin, *Nat. Rev. Mater.* **2019**, *4*, 4.

[4] C. C. Stoumpos, D. H. Cao, D. J. Clark, J. Young, J. M. Rondinelli, J. I. Jang, J. T. Hupp, M. G. Kanatzidis, *Chem. Mater.* **2016**, *28*, 2852.

[5] M. Saliba, J. P. Correa-Baena, M. Grätzel, A. Hagfeldt, A. Abate, *Angew. Chem., Int. Ed.* **2018**, *57*, 2554.

[6] L. Liu, Y. Bai, X. Zhang, Y. Shang, C. Wang, H. Wang, C. Zhu, C. Hu, J. Wu, H. Zhou, Y. Li, S. Yang, Z. Ning, Q. Chen, *Angew. Chem., Int. Ed.* **2020**, *59*, 5979.

[7] N. Liu, P. Liu, H. Ren, H. Xie, N. Zhou, Y. Gao, Y. Li, H. Zhou, Y. Bai, Q. Chen, *ACS Appl. Mater. Interfaces* **2020**, *12*, 3127.

[8] Y. Wang, Y. Liu, S. Cao, J. Wang, *J. Mater. Chem. C* **2021**, *9*, 5302.

[9] R. Ollearo, J. Wang, M. J. Dyson, C. H. L. Weijtens, M. Fattori, B. T. Van Gorkom, A. J. J. M. Van Breemen, S. C. J. Meskers, R. A. J. Janssen, G. H. Gelinck, *Nat. Commun.* **2021**, *12*, 7277.

[10] J. Tong, Q. Jiang, F. Zhang, S. B. Kang, D. H. Kim, K. Zhu, *ACS Energy Lett.* **2021**, *6*, 232.

[11] D. Ma, K. Lin, Y. Dong, H. Choubisa, A. H. Proppe, D. Wu, Y.-K. Wang, B. Chen, P. Li, J. Z. Fan, F. Yuan, A. Johnston, Y. Liu, Y. Kang, Z.-H. Lu, Z. Wei, E. H. Sargent, *Nature* **2021**, *599*, 594.

[12] H. Tsai, W. Nie, J.-C. Blancon, C. C. Stoumpos, R. Asadpour, B. Harutyunyan, A. J. Neukirch, R. Verduzco, J. J. Crochet, S. Tretiak, L. Pedesseau, J. Even, M. A. Alam, G. Gupta, J. Lou, P. M. Ajayan, M. J. Bedzyk, M. G. Kanatzidis, A. D. Mohite, *Nature* **2016**, *536*, 312.

[13] M. Shao, T. Bie, L. Yang, Y. Gao, X. Jin, F. He, N. Zheng, Y. Yu, X. Zhang, *Adv. Mater.* **2022**, *34*, 2107211.

[14] Y. Yang, C. Liu, O. A. Syzgantseva, M. A. Syzgantseva, S. Ma, Y. Ding, M. Cai, X. Liu, S. Dai, M. K. Nazeeruddin, *Adv. Energy Mater.* **2021**, *11*, 2002966.

[15] H. Lai, D. Lu, Z. Xu, N. Zheng, Z. Xie, Y. Liu, *Adv. Mater.* **2020**, *32*, 2001470.

**ADVANCED
SCIENCE NEWS**

www.advancedsciencenews.com

**ADVANCED
MATERIALS**

www.advmat.de

[16] L. Min, W. Tian, F. Cao, J. Guo, L. Li, *Adv. Mater.* **2021**, *33*, 2101714.

[17] Z. Han, W. Fu, Y. Zou, Y. Gu, J. Liu, B. Huang, D. Yu, F. Cao, X. Li, X. Xu, H. Zeng, *Adv. Mater.* **2021**, *33*, 2003852.

[18] J. Kim, W. Lee, K. Cho, H. Ahn, J. Lee, K.-Y. Baek, J.-K. Kim, K. Kang, T. Lee, *Nanotechnology* **2021**, *32*, 185203.

[19] H. L. Loi, J. Cao, X. Guo, C. K. Liu, N. Wang, J. Song, G. Tang, Y. Zhu, F. Yan, *Adv. Sci.* **2020**, *7*, 2000776.

[20] H. Xu, Y. Jiang, T. He, S. Li, H. Wang, Y. Chen, M. Yuan, J. Chen, *Adv. Funct. Mater.* **2019**, *29*, 1807696.

[21] R. Quintero-Bermudez, A. H. Proppe, A. Mahata, P. Todorović, S. O. Kelley, F. De Angelis, E. H. Sargent, *J. Am. Chem. Soc.* **2019**, *141*, 13459.

[22] A. Caiazzo, K. Datta, J. Jiang, M. C. Gélvez-Rueda, J. Li, R. Ollearo, J. M. Vicent-Luna, S. Tao, F. C. Grozema, M. M. Wienk, R. A. J. Janssen, *Adv. Energy Mater.* **2021**, *11*, 2102144.

[23] R. Quintero-Bermudez, A. Gold-Parker, A. H. Proppe, R. Munir, Z. Yang, S. O. Kelley, A. Amassian, M. F. Toney, E. H. Sargent, *Nat. Mater.* **2018**, *17*, 900.

[24] Y. Zhao, C. Li, L. Shen, *Chin. Phys. B* **2018**, *27*, 127806.

[25] Y. Wei, H. Chu, Y. Tian, B. Chen, K. Wu, J. Wang, X. Yang, B. Cai, Y. Zhang, J. Zhao, *Adv. Energy Mater.* **2019**, *9*, 1900612.

[26] Y. Wei, H. Chu, B. Chen, Y. Tian, X. Yang, B. Cai, Y. Zhang, J. Zhao, *Sol. Energy* **2020**, *201*, 13.

[27] C. M. M. Soe, G. P. Nagabhushana, R. Shivaramaiah, H. Tsai, W. Nie, J.-C. Blancon, F. Melkonyan, D. H. Cao, B. Traoré, L. Pedesseau, M. Kepenekian, C. Katan, J. Even, T. J. Marks, A. Navrotsky, A. D. Mohite, C. C. Stoumpos, M. G. Kanatzidis, *Proc. Natl. Acad. Sci. U. S. A.* **2019**, *116*, 58.

[28] Y. Chen, Y. Sun, J. Peng, J. Tang, K. Zheng, Z. Liang, *Adv. Mater.* **2018**, *30*, 1703487.

[29] C. Fuentes-Hernandez, W. F. Chou, T. M. Khan, L. Diniz, J. Lukens, F. A. Larrain, V. A. Rodriguez-Toro, B. Kippelen, *Science* **2020**, *370*, 698.

[30] A. J. J. M. van Breemen, M. Simon, O. Tousignant, S. Shanmugam, J. L. van der Steen, H. B. Akkerman, A. Kronemeijer, W. Ruetten, R. Raaijmakers, L. Alving, J. Jacobs, P. E. Malinowski, F. De Roose, G. H. Gelinck, *npj Flex. Electron.* **2020**, *4*, 22.

[31] W. Yang, W. Qiu, E. Georgitzikis, E. Simoen, J. Serron, J. Lee, I. Lieberman, D. Cheyns, P. Malinowski, J. Genoe, H. Chen, P. Heremans, *ACS Appl. Mater. Interfaces* **2021**, *13*, 16766.

[32] M. Kielar, O. Dhez, G. Pecastaings, A. Curutchet, L. Hirsch, *Sci. Rep.* **2016**, *6*, 39201.

[33] Q. Lin, A. Armin, D. M. Lyons, P. L. Burn, P. Meredith, *Adv. Mater.* **2015**, *27*, 2060.

[34] Y. Fang, J. Huang, *Adv. Mater.* **2015**, *27*, 2804.

[35] J. Wang, K. Datta, J. Li, M. A. Verheijen, D. Zhang, M. M. Wienk, R. A. J. Janssen, *Adv. Energy Mater.* **2020**, *10*, 2000566.

[36] M. Saliba, J.-P. Correa-Baena, C. M. Wolff, M. Stolterfoht, N. Phung, S. Albrecht, D. Neher, A. Abate, *Chem. Mater.* **2018**, *30*, 4193.

[37] A. J. J. M. van Breemen, R. Ollearo, S. Shanmugam, B. Peeters, L. C. J. M. Peters, R. L. van de Ketterij, I. Katsouras, H. B. Akkerman, C. H. Frijters, F. Di Giacomo, S. Veenstra, R. Andriessen, R. A. J. Janssen, E. A. Meulenkamp, G. H. Gelinck, *Nat. Electron.* **2021**, *4*, 818.

**2205261 (9 of 9)**